CONSTRUCTION OF GROUND MOTION EVALUATION MODELS USING SUPERVISED MACHINE LEARNING BASED ON STRONG MOTION DATABASE

Atsuko OANA[1], Toru ISHII[2], Yuki MIYASHITA[3] and Kei FURUKAWA[4]

[1] Member, Dr. Eng., Research Engineer, Institute of Technology, Shimizu Corporation, Tokyo, Japan, a.oana@shimz.co.jp
[2] Member, Dr. Eng., Senior Research Expert, Institute of Technology, Shimizu Corporation, Tokyo, Japan, tokyo@shimz.co.jp
[3] Research Engineer, Dr. Eng., Institute of Technology, Shimizu Corporation, Tokyo, Japan, y-miyashita@shimz.co.jp
[4] Senior Research Engineer, M. Eng., Institute of Technology, Shimizu Corporation, Tokyo, Japan, k.furukawa@shimz.co.jp

ABSTRACT: We constructed ground motion evaluation models of peak accelerations and response spectra using supervised machine learning based on a strong motion database. The common logarithmic standard deviations of the ratios of the predicted values to the observed ones in our models were 0.18–0.21; the variation here is less than that in previous ground motion prediction equations. The generalizability of the models was tested on the data of three earthquakes that occurred after the earthquakes used for the training dataset. The results showed that the prediction accuracy decreased for earthquakes with features that were not included in the training dataset; however, the models with features based on prediction results using the previous ground motion prediction equation could compensate for the bias and lack of training data.

Keywords: *Machine learning, Ground motion prediction, Strong motion database, Peak ground acceleration, Response spectrum*

1. INTRODUCTION

Recently, pioneering studies have been conducted in the fields of seismology and earthquake engineering using machine learning leading to significant advances. Various proposals have been made to improve prediction accuracy and gain new insights by incorporating machine learning approaches in earthquake ground motion prediction and utilizing the observation records accumulated to date. Okazaki et al.[1] created a site-specific ground motion prediction model for peak ground accelerations using neural networks. Kubo et al.[2] proposed a hybrid model based on conventional seismological physics and machine learning. This model was created based on a random forest algorithm using the residuals between the prediction results of the previous ground motion prediction equation (GMPE) and the observation records as training data. In these studies, the same parameters as in conventional GMPEs,

such as magnitude, epicentral distance, focal depth, average S-wave velocity in the upper 30 m ($AVS30$), and top depth of the 1400 m/s S-wave velocity layer (D_{1400}), were used as the features (explanatory variables).

However, to further improve the accuracy of ground motion prediction, common sense and preconceptions in seismology and earthquake engineering should be replaced with additional parameters that can utilize the ability of machine learning to reflect the nonlinear interrelationships of multiple parameters. Matsuoka and Ohno[3] constructed ground motion prediction models using a neural network for response spectra, incorporating the aforementioned parameters, as well as epicenter and observation station locations, as features, and showed that the models demonstrated less variability than previous GMPEs. Oana et al.[4] organized additional features such as epicenter location, observation station location, decision flag for volcanic front passage, and the rupture directivity effect. Then, they created ground motion evaluation models using machine learning based on gradient boosting decision trees for the peak ground acceleration and response spectra.

In this study, first, the training dataset from our previous studies[4, 5] was expanded and developed. Next, we upgraded the ground motion evaluation models using machine learning, making maximum use of the strong ground motion data available at present, and verified the prediction accuracy of the models. Then, the generalizability of the model was verified using additional test data from earthquakes that occurred after the earthquakes included in the training dataset. The distinctive features of this study are that it uses a larger number of parameters than conventional GMPEs and models and proposes an approach for adding the prediction results from a previous GMPE as one of the features.

Hereinafter, the mean values mentioned in this paper are the common logarithmic mean. The same applies to standard deviations.

2. TRAINING DATASET

Strong motion data in the strong motion unified database by Morikawa et al.[6] was used as the training dataset. This database is a tabular compilation of strong motion records obtained by K-NET and KiK-net[7], the strong motion observation networks of the National Research Institute for Earth Science and
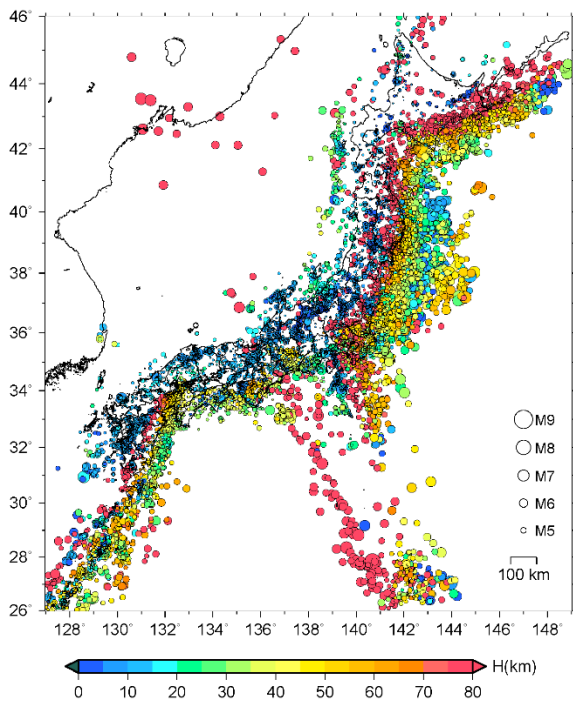

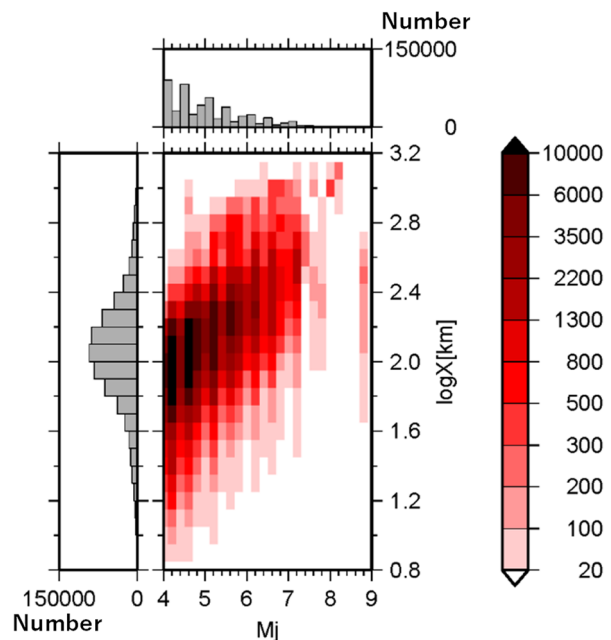Fig. 1 Distribution of earthquake epicenters in the training dataset

Fig. 2 Heatmap of M_J and $\log_{10}X_{min}$ in the training dataset

Disaster Resilience (NIED), from 1997 to February 2018. The database includes the latitude and longitude of the epicenter, Japanese Meteorological Agency (JMA) magnitude, moment magnitude, focal depth, focal mechanism (strike, dip, and slip angles), and classification value of earthquake type by Morikawa and Fujiwara[8] as source information. The database also includes observation station information such as station cord, latitude and longitude of the station, average S-wave velocity in the upper 10 and 30 m, top depth of the 1100, 1400, 1700, and 2100 m/s S-wave velocity layers, and top depth of the seismic bedrock. In addition, the database includes fault distance (for major earthquakes for which source inversion analysis was performed, the fault distance was calculated using the fault model) or hypocentral distance and the classification value of surface and subsurface records. Based on the strong motion records, the peak ground acceleration, peak ground velocity, seismic intensity, and acceleration response spectra (period range: 0.02–20s) at 5% damping of the horizontal and vertical components are calculated and compiled into the database. The soundness of the waveform, such as the signal-to-noise ratio of the Fourier amplitude spectrum, has not been evaluated, nor have filtering processes in the frequency and time domains.

In this study, approximately 630,000 strong motions (14,611 earthquakes) with a peak ground acceleration of 1 cm/s^2 or greater in the horizontal component of the surface record were used as the training dataset. The distribution of epicenters in the training dataset is shown in Fig. 1, a heat map of the JMA magnitude M_J and the logarithm of the fault distance X_{min} ($\log_{10}X_{min}$) is shown in Fig. 2, and the number of data points for each earthquake type is shown in Fig. 3. Figure 1 indicates that earthquakes with a focal depth H of approximately 30–50 km are distributed along the plate boundary around Japan, whereas shallow earthquakes with depths of approximately 20 km or less and deep earthquakes with depths of approximately 60 km or more are distributed inland. Figure 2 implies that there are a few data points with a large M_J and short X_{min} (0–20 are not colored in the figure). However, for example, data with M_J around seven include data with X_{min} shorter than 10 km. Data of earthquakes with M_J less than four also include in the database. Figure 3 indicates that the number of strong motion observation records of plate boundary earthquakes is larger than that of crustal and intra-slab earthquakes. Although it is considered necessary to take measures against such a bias in data distribution in the future, no such measures are taken in this study.

3. MACHINE LEARNING METHOD

Supervised machine learning was used to construct the ground motion evaluation models with the expectation that nonlinear interrelationships among multiple parameters would be reflected. A gradient boosting decision tree[9] was used as the machine learning algorithm because it can sequentially add new weak learners to fill in the difference between the true and predicted values and eventually use all of these weak learners for prediction. This method is expected to be more accurate than the independent decision tree or random forest approaches. A conceptual diagram of the gradient boosting decision tree is shown in Fig. 4. In this study, we used DataRobot[10], a machine learning software that implements XGBoost (eXtreme Gradient Boosting)[11]. Table 1 shows the XGBoost parameters used. The early stopping technique was applied to avoid overfitting. Eighty percent of the training dataset was divided into five parts; four of them (i.e., 64% of the training dataset) were used as teaching data for model creation and one as validation data for evaluating the accuracy of the model. A cross-validation test with five test repetitions was performed. The remaining 20% of the dataset was used as test data to evaluate the generalizability of the model. Teaching, validation, and test data were all selected randomly.

4. OBJECTIVE VARIABLES AND FEATURES IN THE TRAINING DATASET

4.1 Objective variables and candidate features

The objective variables used were peak ground acceleration PGA[cm/s^2] and acceleration response spectra S_A at 5% damping for the period range of 0.02–5s. S_A for the period longer than 5 s was excluded due to the possible influence of long-period noise in the time history. The period points for S_A were 0.02,
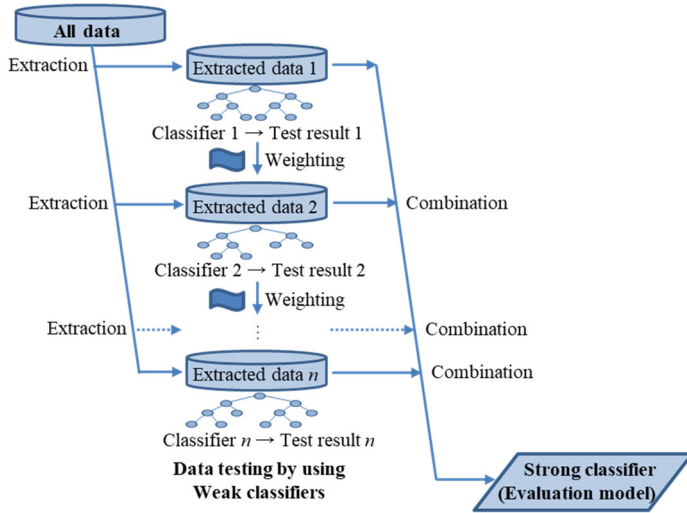
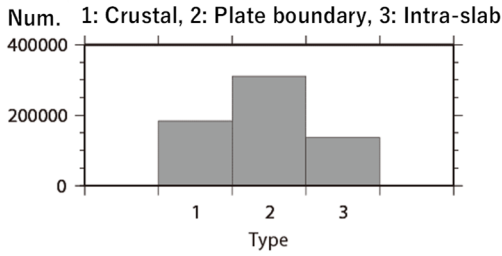Fig. 4 Conceptual diagram of gradient boosting decision tree

Fig. 3 Strong motion observation records for each earthquake type

Table 1 Parameters of XGBoost

| objective (Loss function)	least-squares loss
num_round (Number of boosting stages)	2500
max_depth (Maxmum depth of the individual decision tree)	7
learning_rate (Learnig rate)	0.05
min_child_weight (Minimum sum of instance weight needed in a child)	1.0
colsample_bytree (Subsample ratio of columns when constructing each tree)	0.3
subsample (Subsample ration of the training instances)	1.0
reg_alpha (L1 regularization term on weights)	0.0
reg_lambda (L2 regularization term on weights)	1.0
gamma (Minimum loss reduction required to make a further partition on a leaf node of the tree)	0.01
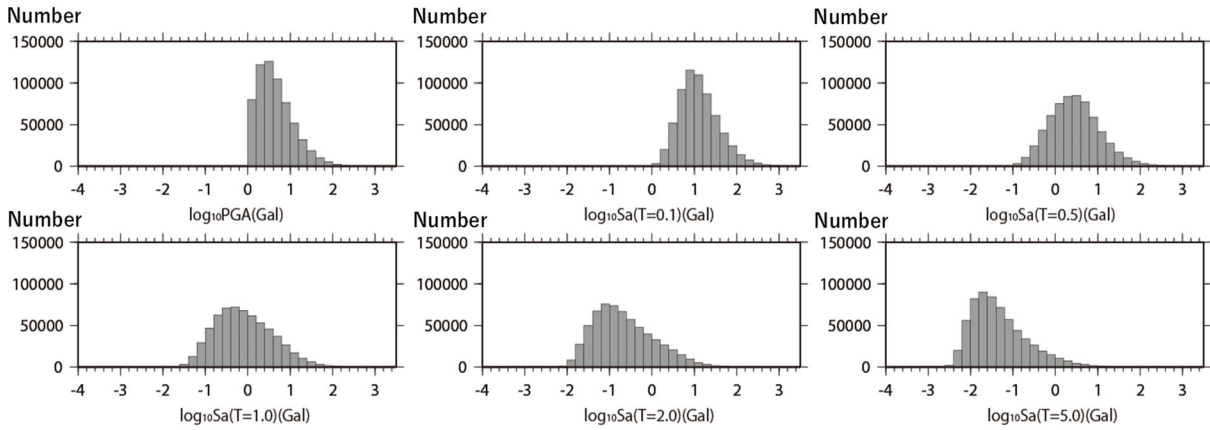
Fig. 5 Example histograms of the objective variables

0.05, 0.1, 0.2, 0.3, 0.4, 0.5, 0.6, 0.7, 0.8, 0.9, 1.0, 1.2, 1.5, 2.0, 2.2, 2.5, 3.0, 3.5, 4.0, 4.5, and 5.0. The models were trained on the common logarithm of RotD50 for PGA ($\log_{10}PGA$) and that of RotD100 for S_A ($\log_{10}S_A$). Examples of the histograms of the objective variables are shown in Fig. 5. The PGA distribution is cut off at 1 cm/s² because PGA is targeted over 1 cm/s². The $\log_{10}S_A$ are almost normally distributed for the period range of 0.1–0.5s, but the centers of the distributions shift toward the small amplitude side for longer periods.

The 20 candidate features are as follows: JMA magnitude M_J, fault distance or hypocentral distance X_{min}[km] (given as $\log_{10}X_{min}$), focal depth H[km], latitude and longitude of the epicenter lat_eq [deg]/lon_eq[deg], earthquake type $Type$, latitude and longitude of the observation station

lat_site[deg]/*lon_site*[deg], S-wave velocity of the uppermost layer *VS1* [m/s], average S-wave velocity in the upper 10 m *AVS10* [m/s], average S-wave velocity in the upper 30 m *AVS30* [m/s], top depth of the 1100 m/s S-wave velocity layer D_{1100} [m], top depth of the 1400 m/s S-wave velocity layer D_{1400} [m], top depth of the 1700 m/s S-wave velocity layer D_{1700} [m], top depth of the 2100 m/s S-wave velocity layer D_{2100} [m], top depth of the seismic bedrock D_{base} [m], epicentral azimuth $Λ$ [deg] (given as sin $Λ$ and cos $Λ$)[12], decision flag for volcanic front passage X_{vflg}[4], and the rupture directivity effect *Dir*[4]. M_J was chosen rather than moment magnitude M_W to utilize data from earthquakes for which the source mechanism and M_W are not available. *VS1* was defined by referring to nearby boring data[13] for some stations where *VS1* was unknown due to lack of data. *AVS30* was used instead of *AVS10* at stations where

Table 2 List of earthquakes for which the fault distance and rupture directivity effect are considered.

Date and time of earthquake	Epicenter	M_J	H[km]	DB*	Reference
1996/10/19 23:44	Hyuganada	6.9	34	○	14)
1996/12/03 07:18	Hyuganada	6.7	38	○	14)
1997/03/26 17:31	Satsuma, Kagoshima	6.6	12	○	15)
1997/05/13 14:38	Satsuma, Kagoshima	6.4	9	○	15)
1997/06/25 18:50	Central Yamaguchi	6.6	8	○	16)
1998/09/03 16:58	Northern Iwate	6.2	8	○	16)
2000/10/06 13:30	Western Tottori	7.3	9	○	17)
2001/03/24 15:28	Akinada Sea	6.7	46	○	18)
2003/05/26 18:24	Off the coast of Miyagi	7.1	72		19)
2003/07/26 07:13	Northern Miyagi	6.4	12		20)
2003/09/26 04:50	Off the coast of Tokachi	8.0	45	○	21)
2004/09/05 19:07	Off the southeast coast of Mie	7.1	38		22)
2004/09/05 23:57	Off the southeast coast of Mie	7.4	44		22)
2004/10/23 17:56	Niigata-Chuetsu	6.8	13	○	23)
2005/03/20 10:53	Off the northwest coast of Fukuoka	7.0	9	○	24)
2007/03/25 09:42	Off the Noto Peninsula	6.9	11	○	25)
2007/07/16 10:13	Off the coast of Niigata-jouchuetsu	6.8	17	○	26)
2008/06/14 08:43	Southern Iwate	7.2	8	○	27)
2008/07/24 00:26	Northern coast of Iwate	6.8	108		28)
2009/08/11 05:07	Suruga-bay	6.5	23		29)
2011/03/11 14:46	Off the coast of Sanriku	9.0	24	○	30)
2011/03/11 15:15	Off the coast of Ibaraki	7.6	43		31)
2011/03/12 03:59	Northern Nagano	6.7	8		32)
2011/04/07 23:32	Off the coast of Miyagi	7.2	66		33)
2011/04/11 17:16	Hamadori, Fukushima	7.0	6		34)
2013/02/25 16:23	Northern Tochigi	6.3	3		35)
2014/11/22 22:08	Northern Nagano	6.7	5		36)
2015/05/13 06:13	Off the coast of Miyagi	6.8	46		37)
2016/01/14 12:25	Off the coast of Urakawa	6.7	52		38)
2016/04/01 11:39	Off the southeast coast of Mie	6.5	29		39)
2016/04/14 21:26	Kumamoto	6.5	11		40)
2016/04/16 01:25	Kumamoto	7.3	12	○	41)
2016/10/21 14:07	Central Tottori	6.6	11		42)
2016/11/22 05:59	Off the coast of Fukushima	7.4	25		43)

*The earthquakes to which the source model was originally reffered when the strong motion database was created are marked with "○".

AVS10 could not be obtained. Table 2 shows the list of earthquakes for which the fault distance and rupture directivity effect are considered. No trimming or other editing was performed on the source inversion results. X_{min} for earthquakes not shown in Table 2 was the hypocentral distance. Because *Dir* is defined as a measure of the relative rupture directivity effect at each station within the earthquake, *Dir* for earthquakes not shown in Table 2 was uniformly taken to be 0.5, assuming rupture from the center of the circular fault plane.

If features are dependent on each other, not only will their influence on the objective variable be distributed, and thus difficult to interpret, but there is also the concern of overfitting in machine learning. Therefore, it is preferred that the features be independent of each other. First, the mutual information values among the features were compiled, as shown in Fig. 6. Hereinafter, the values in parentheses indicate the mutual information. $\sin \varLambda$ and $\cos \varLambda$ (0.63) are naturally highly correlated because they share commonality through $\varLambda$. The reason for the high mutual information values of D_{1700} and D_{2100} (0.59), D_{1400} and D_{1700} (0.47), D_{1100} and D_{1400} (0.44), D_{1400} and D_{2100} (0.42), D_{2100} and D_{base} (0.41), D_{1100} and D_{1700} (0.37), D_{1700} and D_{base} (0.36), and D_{1100} and D_{2100} (0.33) may be due to the correlation derived from the thickness of each layer consisting of the deep soil structure. The relationship between *H* and *Type* (0.39) appears to reflect a bias in the location of the earthquake and its focal depth. The relationships between *lat_eq* and *lon_eq* (0.36) and *lat_site* and *lon_site* (0.36) are not physical correlations, as they are due to the distribution of epicenters and observation stations along the topography of the Japanese archipelago, which extends in the northeast-southwest direction.

4.2 Influence of the number of features

To confirm the influence of the number of features, ground motion evaluation models with different numbers of features were constructed for *PGA* as a representative example. Models M20–M5 (the number in the model name corresponds to the number of features used in that model) were constructed by individually removing first the features with high mutual information values and then features with low influence on the prediction results. Subsequently, validations were performed for each model, and the proximity between the predicted values of each model and the observed values was evaluated.
The impact of each feature in Model M20 is shown in Fig. 7. Here, Permutation Importance[44] was used as the feature impact. The large impacts of X_{min}, M_J, and *H* provide the rationale for these parameters being mainly used in previous GMPEs. Following them, the impacts of *lon_eq*, *lat_eq*, *lon_site*, and *lat_site* are nearly as large as *H*. The regional source characteristics are affected by the epicenter location, whereas the site characteristics are affected by the site location. Therefore, it is inferred that those effects are reflected in the feature impact[45]. Moreover, following them, the impacts of *AVS10* and D_{base} are relatively large, whereas the impacts of other features are small with similar ratios.

Models M20–M5 and their features are shown in Table 3. The cross-validation and test results for each model are shown in Table 4. Table 4 also shows the means and standard deviations of the common logarithm of the ratio distributions of the predicted values to the observed ones. Here, the normalized Gini, which evaluates the consistency between the rank order of the observations and that of the predictions when sorted in order of increasing amplitude, was used as the evaluation index for the cross-validations and tests. If the normalized Gini value is one, the observed and predicted ranks are in perfect agreement. Table 4 shows that the cross-validation and test results for M20–M16 are greater than 0.9, with a mean of zero and a small standard deviation, suggesting a high prediction accuracy. However, the validation and test results values decrease slightly, and the standard deviations increase slightly for models with less than 15 features. The increase rate of the standard deviation is particularly large for Models M8–M5. Sammon mapping[46], which evaluates the proximity between predicted and observed values, is shown in Fig. 8. The figure indicates that M16–M20 are relatively close to the observed values ("obs"), whereas the other models are further away from the observed values. This visually indicates the same trend as in the validation and test results. Considering the above, we concluded that approximately 16 features in the ground motion evaluation model for our dataset would provide sufficient prediction accuracy.

As a result, the following 16 features were selected for machine learning: M_J, X_{min}, *H*, *lat_eq*, *lon_eq*, *lat_site*, *lon_site*, *VS1*, *AVS10*, *AVS30*, D_{1400}, D_{base}, $\sin\varLambda$, $\cos\varLambda$, X_{vflg}, and *Dir*.
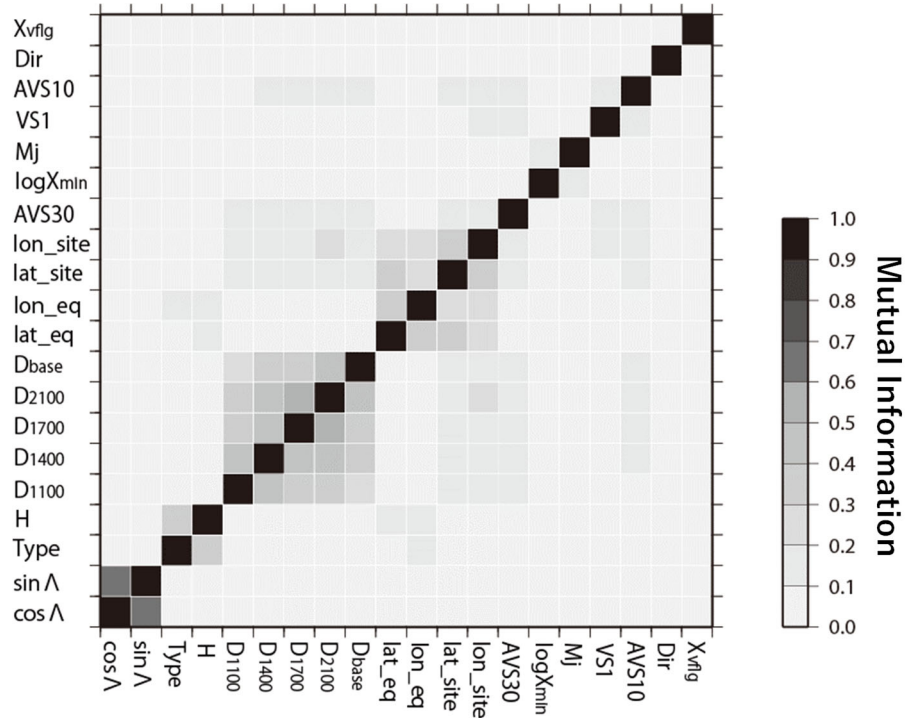
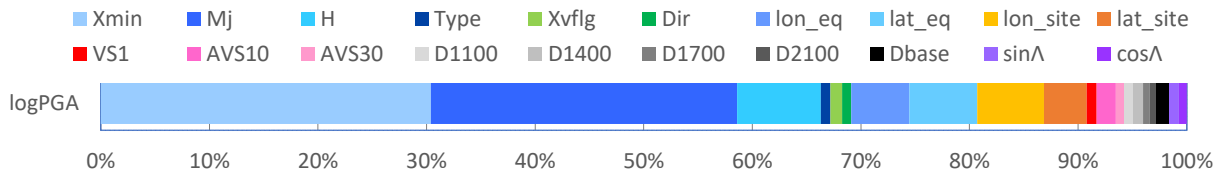Fig. 6 Mutual information values among the features

Fig. 7 Impact of each feature in Model M20; the horizontal axis is standardized so that the sum of the feature impact is 100%.

Table 3 Models M20–M5 and their features

Feature / Model	M20	M19	M18	M17	M16	M15	M14	M13	M12	M11	M10	M9	M8	M7	M6	M5	M17MF
Xmin	○	○	○	○	○	○	○	○	○	○	○	○	○	○	○	○	○
Mj	○	○	○	○	○	○	○	○	○	○	○	○	○	○	○	○	○
H	○	○	○	○	○	○	○	○	○	○	○	○	○	○	○	○	○
lat_eq	○	○	○	○	○	○	○	○	○	○	○	○	○	○	○	○	○
lon_site	○	○	○	○	○	○	○	○	○	○	○	○	○	○	○	○	○
lon_eq	○	○	○	○	○	○	○	○	○	○	○	○	○	○	○		○
lat_site	○	○	○	○	○	○	○	○	○	○	○	○	○	○			○
AVS10	○	○	○	○	○	○	○	○	○	○	○	○	○				○
Dbase	○	○	○	○	○	○	○	○	○	○	○	○					○
Xvflg	○	○	○	○	○	○	○	○	○	○	○						○
D1400	○	○	○	○	○	○	○	○	○	○							○
VS1	○	○	○	○	○	○	○	○	○								○
sinΛ	○	○	○	○	○	○	○	○									○
Dir	○	○	○	○	○	○	○										○
AVS30	○	○	○	○	○	○											○
cosΛ	○	○	○	○	○												○
Type	○	○	○	○													
D2100	○	○	○														
D1100	○	○															
D1700	○																
MF13																	○

Table 4 Cross-validation and test results for each model

	M20	M19	M18	M17	M16	M15	M14	M13	M12	M11	M10	M9	M8	M7	M6	M5	M17MF
Cross-validation	0.904	0.904	0.902	0.902	0.903	0.898	0.899	0.900	0.893	0.894	0.895	0.896	0.876	0.860	0.825	0.746	0.901
Test	0.903	0.904	0.902	0.902	0.903	0.897	0.898	0.900	0.892	0.893	0.895	0.896	0.875	0.860	0.822	0.744	0.900
Mean	0.000	0.000	0.000	0.000	0.000	0.000	0.000	0.000	0.000	0.000	0.000	0.000	0.000	0.000	0.000	0.000	0.000
Standard deviation	0.177	0.176	0.178	0.178	0.177	0.181	0.181	0.179	0.186	0.185	0.184	0.183	0.199	0.209	0.231	0.280	0.178
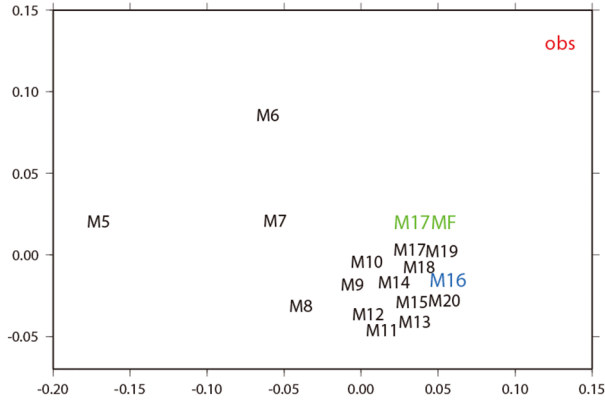
Fig. 8 Sammon mapping evaluating the proximity between predicted and observed values

(a) M16

(b) M17MF

(The horizontal axis value means the period of S_A.)
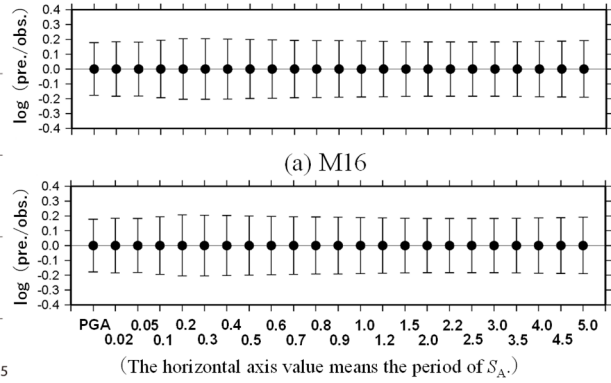
Fig. 9 Means and standard deviations of the common logarithm of the ratio distributions of the predicted values to the observed ones for the training dataset

5. CONSTRUCTION OF GROUND MOTION EVALUATION MODELS

5.1 Ground motion evaluation Model M16

The ground motion evaluation Model M16 for PGA and S_A (for the period range 0.02–5 s) at 5% damping was constructed with machine learning using the features listed in Table 3. The means and standard deviations of the common logarithm of the ratio distributions of the predicted values to the observed ones for the training dataset are shown in Fig. 9(a). The means were zero for all the ground motion indexes, and the standard deviations were in the range 0.18–0.20 and were smaller than those of the previous GMPEs[8), 47)]. The examples of the relationships between observed and predicted values shown in Fig. 10 indicate that there is no significant difference between the ratio distributions of the training and cross-validation data and those of the test data. Additionally, the shapes of the ratios of the predicted values to the observed ones are almost normally distributed.

Figure 11(a) shows the feature impacts of Model M16; the proportion of the impact of each feature differs depending on the period. The impact of X_{min} is approximately 30% in the short-period range, but it decreases up to 0.6 s and is approximately 20% in periods over 0.6 s. The impact of M_J is small at approximately 20% for periods of 0.05 s and 0.1s, but generally increases as the period becomes longer, reaching more than 50% for periods over 1s. The impact of H is slightly less than 10% for the period range of 0.02–0.1 s, decreases slightly for the period range of 0.2–0.5 s, and is almost the same proportion for periods over 0.5 s. The impacts of *lon_eq*, *lat_eq*, *lon_site*, and *lat_site* are smaller for longer periods. The impacts of the shallow ground features are larger in the order of *AVS10*, *VS1*, and *AVS30* in the whole period range, where they are most likely to have an influence. The sum of the impacts of these three features contributes more than 5% for the period range of 0.2–1.5 s, but is less significant for the periods under 0.1 s. The respective impacts of D_{1400} and D_{base} are small independent of periods; the sum of the impacts of two features is approximately 3–4%of the total. The impacts of $\sin \Lambda$ and $\cos \Lambda$ are only a few percent regardless of the period. The impact of X_{vflg} contributes only a few percent, but its effect is relatively large in the short-period range. The impact of *Dir* tends to increase with longer periods,
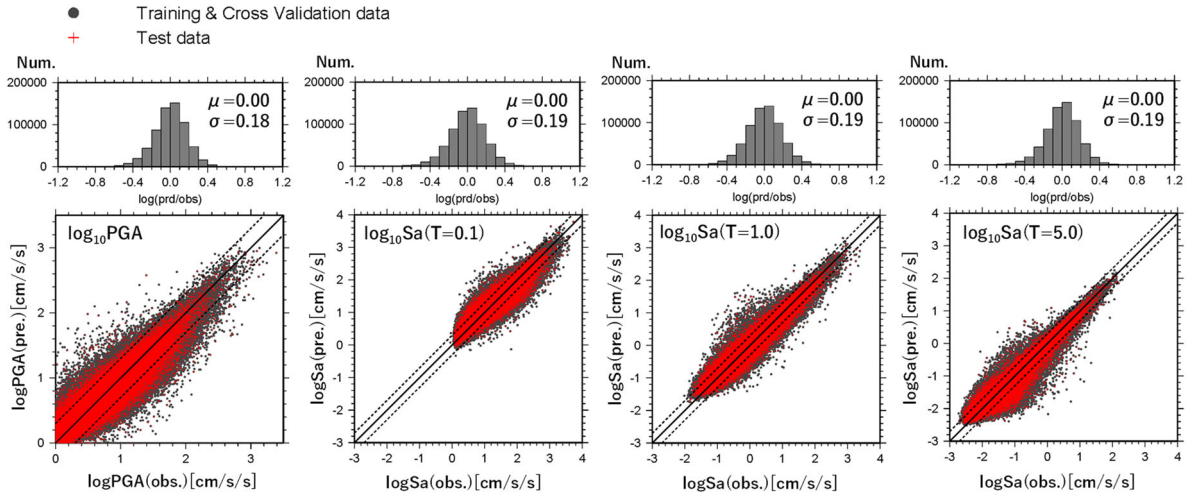
Fig. 10 Examples of the relationships between observed and predicted values; the solid lines indicate one times the observed values, and the dashed lines indicate half and twice the observed values.
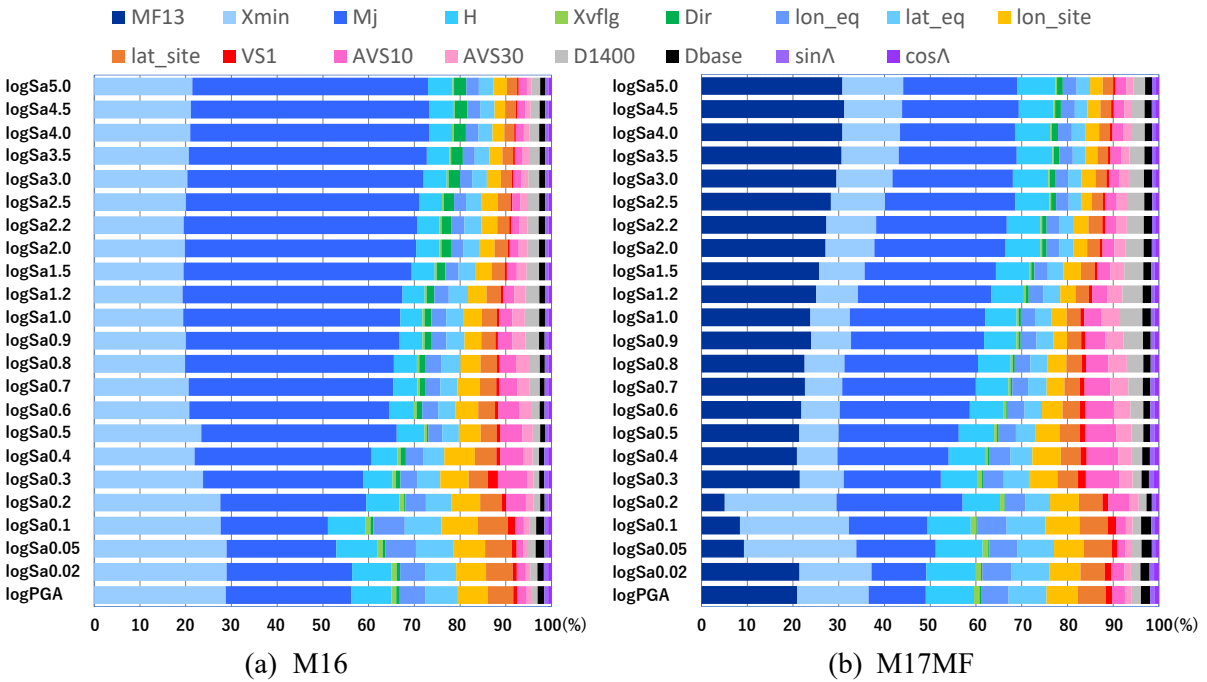

(a) M16　　　　　　　　　　　(b) M17MF

Fig. 11 Feature impacts in Models M16 and M17MF; the horizontal axis is standardized so that the sum of the feature impact is 100%.

accounting for 3% for periods over 3 s, and is comparable to that of the features for shallow and deep underground structures. All feature impacts were positive values; thus, no features were completely insignificant.

5.2　Ground motion evaluation Model M17MF

As in the study by Ishii et al.[5], the prediction result from the previous GMPE was added to the 16 features in the previous section as a new feature, and machine learning was performed again to examine its effects on the ground motion evaluation models.

The equation formulated by Morikawa and Fujiwara[8] was used for the GMPE. Here, the Model 1 equation with a term of the square of M_W is used, where the value obtained is the vector of the two

horizontal components of the ground motion. For $M_W < 5.5$, the GMPE is extrapolated, and when M_W is unknown, it is converted from M_J to M_W using Takemura's[48] equation. Correction terms for amplification characteristics and anomalous seismic intensity distribution were not considered. The predicted result (denoted as feature *MF13*) was added to the M16 features to construct the ground motion evaluation models M17MF for *PGA* and S_A (for the period range of 0.02–5 s) at 5% damping using machine learning (refer to M17MF in Table 3). Note that the prediction results of the GMPE[8] are the results of using some of the other features of the M17MF, thus, the effects of those features are double counted.

Table 4 shows that the scores of M17MF in the cross-validation and test are comparable to those of M16. As shown in Fig. 8, the distance to the observations in the *PGA* is slightly closer for M17MF than for M16, suggesting that M17MF reproduces the observations more accurately. As shown in Fig. 9(b), the means of the common logarithm of the ratio distributions of the predicted values to the observed ones for the training dataset were zero for all ground motion indexes. The standard deviations were 0.18–0.21, and were similar to those of M16 and smaller than those of previous GMPEs[8, 47].

The feature impacts of Model M17MF are shown in Fig. 11(b). Compared with M16 in Fig. 11(a), a considerable amount of the impact of M_J and X_{min} is replaced by MF13, and the impact of the other features increases slightly except for *Dir*, which suggests that the double counting of feature effects has little influence. There is a gap between the period of 0.2 s and 0.3 s. In the period range of 0.05–0.2 s, the impacts of *MF13*, *AVS10*, and *AVS30* are small, while those of *lon_eq*, *lat_eq*, *lon_site*, and *lat_site* are relatively large. The GMPE[8] also has large residuals in this period range, suggesting that the influences of not only the shallow and deep soil structures below the site but also the regional characteristics of the hypocenter and observation stations, or unexpected features, may be strong in this period range. As in the case of M16, all the feature impacts were positive values; thus, no feature were completely insignificant.

6. VALIDATIONS USING ADDITIONAL TEST DATA

In the previous section, we verified the generalizability of the models using 20% test data randomly selected from the training dataset. However, to validate the accuracy of the model for the prediction problem, the test data should be from earthquakes that occurred later than the training data. In this section, we used the strong motion data from the 2018 northern Osaka earthquake, 2019 off the coast of Yamagata earthquake, and 2021 off the coast of Fukushima earthquakes (hereinafter referred to as the Osaka earthquake, Yamagata earthquake, and Fukushima earthquake, respectively.) as additional test data, which are not included in the training dataset, to further validate the generalizability of the models. The predicted values were compared to the observed ones to validate the prediction accuracy of M16 and M17MF. The characteristics[49] of the three earthquakes used as additional test data are shown in Fig. 12. The source inversion results from Asano et al.[50], NIED[51], and Kubo et al.[52] were used to calculate X_{min} and *Dir* for each earthquake. As in the training dataset, the objective observation stations were those with *PGA* of RotD50 over 1 cm/s^2.

Comparisons of the attenuation characteristics of *PGA* predictions and observations for the three earthquakes for Models M16 and M17MF are shown in Fig. 13. For the Osaka earthquake, the M16 predictions sufficiently capture the trend of observed attenuation. The observed and predicted values correspond well for the M17MF, except for a slight underestimation at the fault distance of around 50 km. For the Fukushima earthquake, both models show relatively good correlation between observed and predicted values. For the Yamagata earthquake, the underestimation of the predictions in the range of 50–200 km is noticeable in both models. AKTH04 (Higashinaruse), a site where extremely large amplitudes were observed, had amplification approximately five times greater than that of its neighboring stations. Because the AKTH04 seismograph is located on a cliff[53], the topographical effect may have caused the amplification. However, it was also confirmed that not all earthquakes are always greatly amplified. Therefore, it is considered that the machine learning models could not reproduce this trend. Although the accumulation of similar data is ideal for learning such trends in the machine learning models, measures such as weighting unique training data are also considered effective.

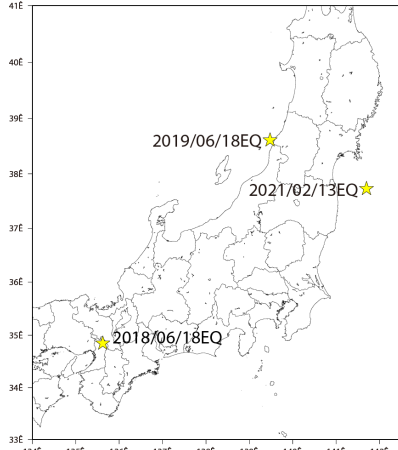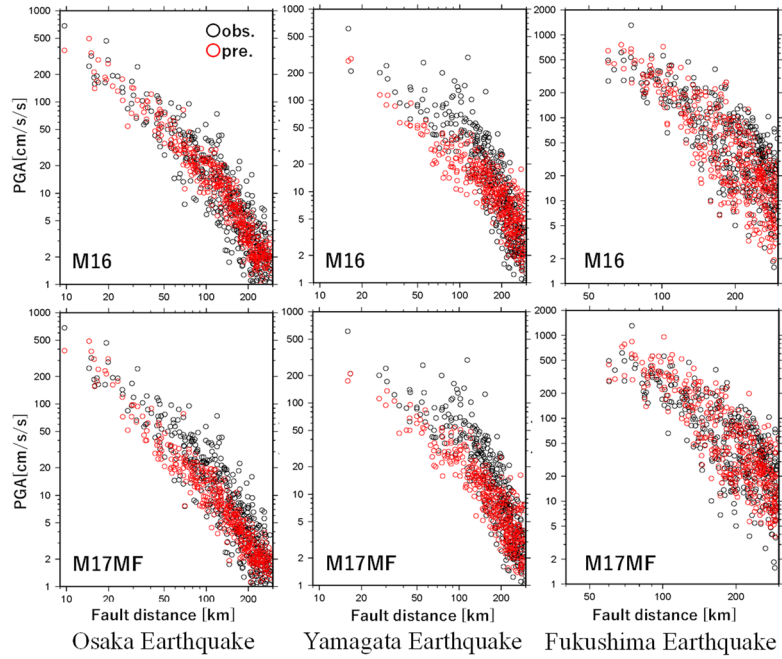| Date and time of earthquake	Epicenter	M_j	H[km]
2018/06/18 07:58	Northern Osaka	6.1	13
2019/06/18 22:22	Off the coast of Yamagata	6.7	14
2021/02/13 23:08	Off the coast of Fukushima	7.3	55

Fig. 12 Properties of earthquakes used as additional test data

Fig. 13 Comparisons of the attenuation of *PGA* predictions and observations for the three earthquakes for Models M16 and M17MF
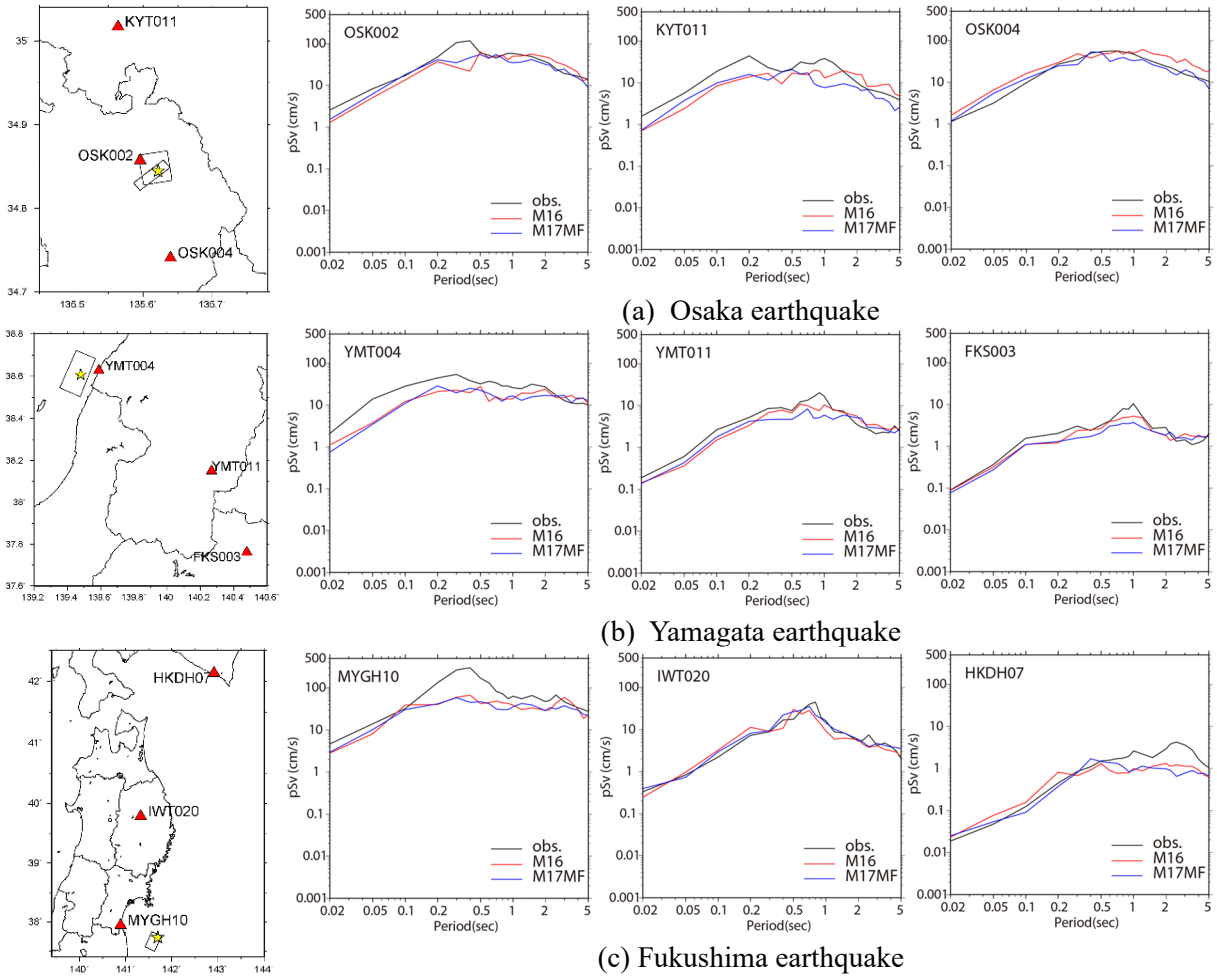
(a) Osaka earthquake

(b) Yamagata earthquake

(c) Fukushima earthquake

Fig. 14 Comparisons of the pseudo-velocity response spectra $_pS_V$ predictions and observations
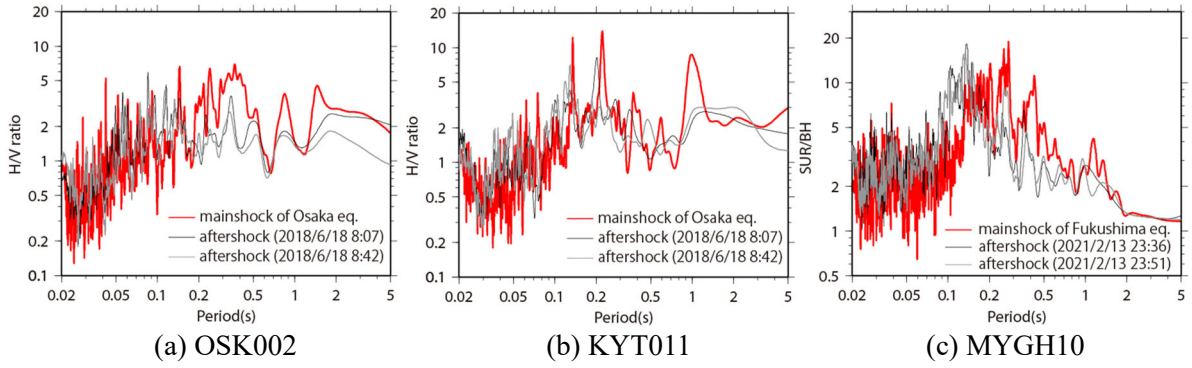
Fig. 15 H/V spectral ratio or surface/borehole spectral ratio of the observation records for the mainshock and aftershocks

Figure 14 compares the observed pseudo-velocity response spectra $_pS_V$ at 5% damping, calculated by dividing S_A by the circular frequency ω, with the predictions of both models, using the three sites shown on the left side of the figure for each earthquake. In general, the predicted results represent the periodic characteristics of the response spectra of the observation records well. However, the spectral peaks in OSK002, KYT011, and MYGH10 are underestimated at the period range of approximately 0.2–0.5 s, which is considered to be the primary dominant period in the surface ground. The H/V spectral ratios of the OSK002 and KYT011 records for the mainshock and aftershocks are shown in Fig. 15(a) and 15(b) respectively, and the surface/borehole spectral ratio of the record at MYGH10 is shown in Fig. 15(c). Figure 15 shows that there is no significant change in the dominant period between the mainshock and aftershock records for OSK002 and KYT011. However, focusing on the period of approximately 0.2–0.5 s for OSK002 and the period of just over 0.2 s for KYT011, it was clear that the ground motion amplification was greater than that of the aftershocks during the mainshock. In the spectral ratio of the mainshock record at MYGH10, the peak around 0.1 s in the aftershock records shifts to approximately 0.2–0.3 s, and amplification exceeding that of the aftershock records is observed at approximately 0.4–0.6 s. It is inferred that the dataset could not learn the amplitude-dependent ground amplification characteristics because the number of stations with experience of observing large-amplitude ground motions is few in this dataset, and there is almost no data where the dominant period is extended or the amplitude level increases or decreases due to nonlinear behavior of the surface soil. Some modifications of the training data are necessary for such cases. In the Osaka earthquake shown in Fig. 14(a), both M16 and M17MF accurately reproduce the period range of 0.5 s or longer range at OSK002 near the source. At OSK004, M17MF reproduces the observation well for a broadband period, whereas M16 is larger than M17MF for a long period over 1s and overestimates the observation. The tendency for M16 to be larger than M17MF in the long-period range is also apparent in OSK002 and KYT011. This is inferred to be due to the greater influence of $Dir^{4)}$. In the Yamagata earthquake shown in Fig. 14(b), both models underestimate the observations for YMT004 near the source in an approximately 2 s period or less, whereas the results for YMT011 and FKS003 far from the epicenter are in good agreement with the observations for a broadband period. In the Fukushima earthquake shown in Fig. 14(c), both models performed equally well. The prediction results of MYGH10 for the period range of 0.1–2 s are underestimated, although those for the other period ranges are comparable to the observation. The prediction results of IWT020 correspond very well with the observation for a broadband period. The prediction results of HKDH07 are underestimated in the long-period range over approximately 1 s. The response spectrum of the 3 s period was uniquely large in the east of Hokkaido in this earthquake compared to other earthquakes of the same magnitude and type[54]. This earthquake was difficult to represent in the machine learning model because it was a rare event.

The means and standard deviations of the common logarithm of the ratios of the predicted values to the observed ones for the additional test data are shown in Fig. 16 for each earthquake. In the case of the Osaka earthquake, the mean values remarkably exceeded zero for periods over 1 s in the M16, indicating a trend toward overestimation. Such a trend is suppressed in the M17MF, and the plots are distributed around zero in every period. The standard deviations are approximately 0.3 for the period
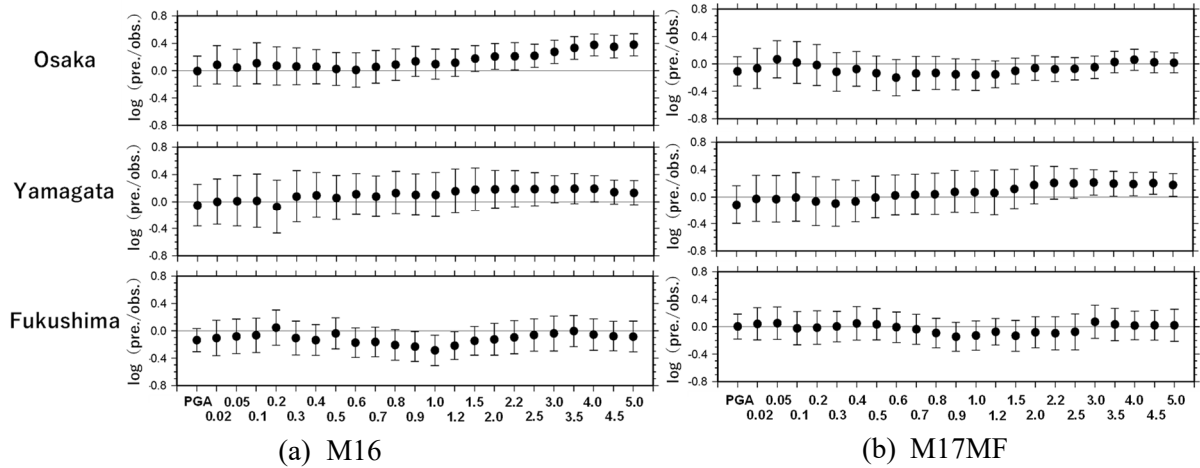
(a) M16   (b) M17MF

Fig. 16 Means and standard deviations of the common logarithm of the ratios of the predicted values to the observed ones for the additional test data; the horizontal axis value is the period of S_A.
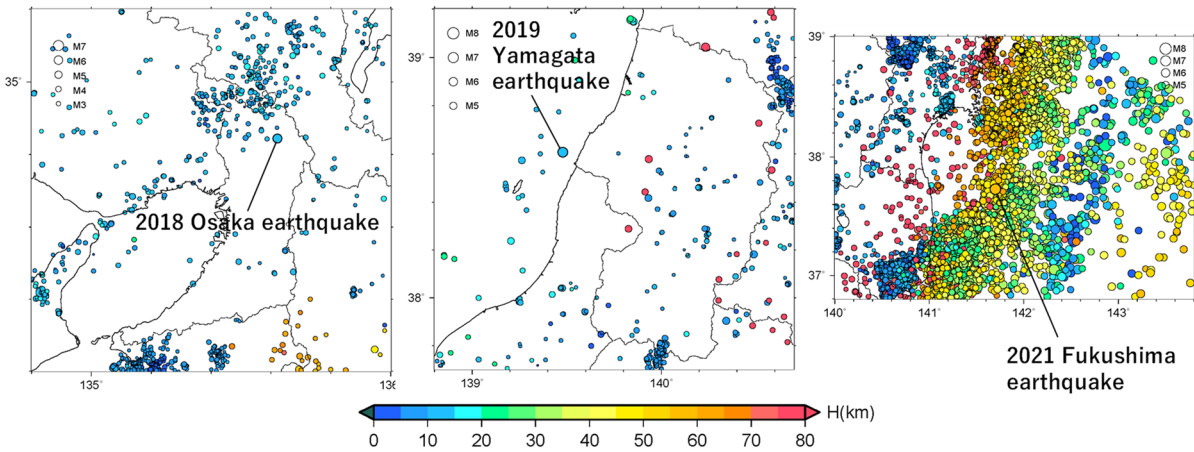

Fig. 17 Epicenter distributions of training dataset around the additional test data earthquakes

range of 0.1–0.3 s, and become smaller for a longer period to approximately 0.15. In the case of the Fukushima earthquake, the mean values of the M16 are smaller than zero for the period range of 0.9–1.2 s. In the M17MF, the plots are distributed around zero in every period, and their standard deviations are as small as 0.18–0.24, which indicates stable and accurate evaluation for a broadband period. The biases and deficiencies in the training data may have been compensated for using the prediction results of the previous GMPE as a feature. In the Yamagata earthquake, the means and standard deviations of two models were similar, and the means were slightly overestimated for the long-period range. The standard deviations became smaller for the longer periods. However, their values were large, in the range of 0.3–0.4 for periods under 2 s, and the prediction accuracy was poor compared to the other two earthquakes. Two reasons for the poor accuracy are the lack of earthquake data on the Japan Sea side in the training dataset and the lack of ground motion data with conditions similar to those of the Yamagata earthquake. Figure 17 shows the epicenter distributions of the training dataset around the additional test data earthquakes. The figure shows that earthquakes of approximately M5 occur densely around the epicenter of the Fukushima earthquake. No earthquakes of the same location and magnitude occurred around the epicenter of the Osaka earthquake, but there were some small earthquakes north to northwest of the epicenter. There were almost no earthquakes in the region around the epicenter of the Yamagata earthquake. Therefore, the constructed models do not sufficiently learn the ground motion characteristics caused by seismic waves propagating along the Japan Sea coast at observation stations in and around the Tohoku region. Such regional data bias is one of the issues of the models in this study. In the future, the lack of data can be compensated by utilizing simulation data, etc.

7. CONCLUSIONS

Using the strong motion database[6], we constructed two ground motion evaluation models for *PGA* and S_A at 5% damping using machine learning (supervised learning) based on gradient boosting decision trees. The first is Model M16, which uses 16 features including the epicenter location and observation station locations, and the second is Model M17MF, which uses 17 features including the features of M16 and the prediction result based on the previous GMPE. The common logarithmic standard deviations of the ratios of the predicted values to the observed ones of the constructed models were 0.18–0.21; these deviations were smaller than the variability of the previous GMPEs.

The generalizability of the models was verified with additional test data, and Model M17MF produced more stable results than Model M16 for a broadband period. Using the result of the previous GMPE as a feature may have compensated for the bias and lack in the training data. Prediction accuracy appeared to be affected by the sparsity and density of the training dataset for each earthquake region. For Model M17MF, in the case of the Fukushima earthquake, the ratios of the predicted values to the observed ones were distributed around zero with a small standard deviation range of 0.18–0.24, due to the rich training data for earthquakes that occurred in that region. In the case of the Osaka earthquake, the ratios of the predicted values to the observed ones were distributed around zero, with standard deviations in the range of 0.15–0.3, due to the relatively limited amount of training data for earthquakes that occurred in that region. In the case of the Yamagata earthquake, because there was almost no training data for earthquakes that occurred in that region, the predicted results were overestimated on average for the long-period range, and the variations were larger than those of the other two earthquakes.

The ground motion evaluation models in this study consider neither the effects of nonlinear behavior of the surface soil on the periodical and amplitude characteristics of ground motions, nor the imbalance of various data distributions. In the future, it is necessary to consider how to compensate for these factors using simulation data. In addition, we intend to develop a less labor-intensive method for evaluating the soundness of the time histories of each of the big ground motion data, and realize the evaluation of the phase characteristics of ground motions and the response spectra for the long-period range of over 5 s.

REFERENCES

1) Okazaki, T., Morikawa, N., Iwaki, A., Fujiwara, H., Iwata, T. and Ueda, N.: Ground-Motion Prediction Model Based on Neural Networks to Extract Site Properties from Observational Records, *Bulletin of the Seismological Society of America*, Vol. 111, No. 4, pp. 1740–1753, 2021. https://doi.org/10.1785/0120200339
2) Kubo, H., Kunugi, T., Suzuki, W., Suzuki S. and Aoi, S.: Hybrid Predictor for Ground-Motion Intensity with Machine Learning and Conventional Ground Motion Prediction Equation, *Scientific Reports*, Vol. 10, No. 11871, 2020. https://doi.org/10.1038/s41598-020-68630-x
3) Matsuoka, K. and Ohno, S.: Study on Ground Motion Spectrum Evaluation Using Machine Learning, *Proceedings of the Annual Meeting of Japan Association for Earthquake Engineering*, B-4-5, 2020 (in Japanese, title translated by the authors).

4) Oana, A., Ishii, T., Miyashita, Y. and Furukawa, K.: Trial of Construction of Ground Motion Evaluation Models by Machine Learning: Study of Features on Volcanic Fronts and Rupture Directivity Effects, *Proceedings of the Annual Meeting of Japan Association for Earthquake Engineering*, T2021-010, 2021 (in Japanese, title translated by the authors).

5) Ishii, T., Oana, A., Miyashita, Y. and Furukawa, K.: Trial Study on the Possibility of Machine Learning Considering the Features Based on the Ground Motion Prediction Equation, *Proceedings of the Annual Meeting of Japan Association for Earthquake Engineering*, T2021-012, 2021 (in Japanese, title translated by the authors).

6) Morikawa, N., Fujiwara, H., Iwaki, A., Maeda, T., Kubo, H., Aoi, S., Kato, K., Tomozawa, Y., Suzuki, F., Sato, T., Ishii, T., Shimazu, N., Miyakoshi, J., Oana, A., Si, H., Hayakawa, T., Hayashi, T., Kishida, N. and Midorikawa, S.: Toward to Construction of Strong-Motion Database for Seismic Hazard Assessment in Japan, *JpGU–AGU Joint Meeting 2020*, SSS04-P01, 2020.

7) National Research Institute for Earth Science and Disaster Resilience, NIED K-NET, KiK-net, *National Research Institute for Earth Science and Disaster Resilience*, 2019. https://www.doi.org/10.17598/NIED.0004

8) Morikawa, N. and Fujiwara, H.: A New Ground Motion Prediction Equation for Japan Applicable up to M9 Mega-Earthquake, *Journal of Disaster Research*, Vol. 8, No. 5, pp. 878–888, 2013. https://doi.org/10.20965/jdr.2013.p0878

9) Friedman, J. H.: Greedy Function Approximation: A Gradient Boosting Machine, *The Annals of Statistics*, Vol. 29, No. 5, pp. 1189–1232, 2001. https://doi.org/10.1214/aos/1013203451

10) DataRobot Inc.: DataRobot. https://app.datarobot.com/ (last accessed on September 1, 2021)

11) Chen, T. and Guestrin, C.: XGBoost: A Scalable Tree Boosting System, *Proceedings of the 22nd ACM SIGKDD International Conference on Knowledge Discovery and Data Mining*, pp. 785–794, 2016.   https://doi.org/10.1145/2939672.2939785

12) Ishii, T., Oana, A. and Wada, K.: An Approach to Obtaining New Insights by Evaluating Ground Motions Using Machine Learning, *Proceedings of the Annual Meeting of Japan Association for Earthquake Engineering*, P1-13, 2019 (in Japanese, title translated by the authors).

13) Tokyo Metropolitan Government Bureau of Construction: Ground of Tokyo (GIS version) (in Japanese). https://www.kensetsu.metro.tokyo.lg.jp/jigyo/tech/start/03-jyouhou/geo-web/00-index.html (last accessed on March 4, 2020)

14) Yagi, Y., Kikuchi, M., Yoshida, S. and Sagiya, T.: Comparison of the Coseismic Rupture with the Aftershock Distribution in the Hyuga-Nada Earthquakes of 1996, *Geophysical Research Letters*, Vol. 26, No. 20, pp. 3161–3164, 1999. https://doi.org/10.1029/1999GL005340

15) Horikawa, H.: Earthquake Doublet in Kagoshima, Japan: Rupture of Asperities in a Stress Shadow, *Bulletin of the Seismological Society of America*, Vol. 91, No. 1, pp. 112–127, 2001. https://doi.org/10.1785/0119990131

16) Miyakoshi, K, Kagawa, T., Sekiguchi, H., Iwata, T. and Irikura, K.: Source Characterization of Inland Earthquakes in Japan Using Source Inversion Results, *Proceedings of 12th World Conference on Earthquake Engineering*, No. 1850, 2000.

17) Sekiguchi, H., Iwata, T., Sugiyama, Y., Fusejima, Y. and Horikawa, H.: Faulting Process and Condition for Its Occurrence of 2000 Tottori-Ken Seibu Earthquake, *2001 Japan Earth and Planetary Science Joint Meeting*, S3-006, 2001.

18) Kakehi, Y: Analysis of the 2001 Geiyo, Japan, Earthquake Using High-Density Strong Ground Motion Data: Detailed Rupture Process of a Slab Earthquake in a Medium with a Large Velocity Contrast, *Journal of Geophysical Research*, Vol. 109, B08306, 2004. https://doi.org/10.1029/2004JB002980

19) Aoi, S., Sekiguchi, H., Kunugi, T., Honda, R. and Fujiwara, H.: Ground Motion and Rupture Process of the 2003 Sanriku-Minami Earthquake Obtained from Strong Motion Data of K-NET and KiK-net, 2003. https://www.kyoshin.bosai.go.jp/kyoshin/topics/miyagi_e/ (last accessed on October 13, 2021)

20) Aoi, S., Sekiguchi, H., Kunugi, T., Honda, R. and Fujiwara, H.: Ground Motion and Rupture Process of the 2003 Northern Miyagi Earthquake Obtained from Strong Motion Data of K-NET

and KiK-net , 2003 (in Japanese, title translated by the authors). https://www.kyoshin.bosai.go.jp/kyoshin/topics/miyagi_200307260713/ (last accessed on October 13, 2021)

21) Koketsu, K., Hikima, K., Miyazaki, S. and Ide, S.: Joint Inversion of Strong Motion and Geodetic Data for the Source Process of the 2003 Tokachi-Oki, Hokkaido, Earthquake, *Earth, Planets and Space*, Vol. 56, No. 3, pp. 329–334, 2004. https://doi.org/10.1186/BF03353060

22) Kanazawa, T.: Earthquake Off the Kii Peninsula (September 5, 2004, M7.1; M7.4), *The 40-Year History of the Coordinating Committee for Earthquake Prediction, Japan*, 2009 (in Japanese, title translated by the authors).

23) Asano, K. and Iwata, T.: Source Rupture Process of the 2004 Chuetsu, Mid-Niigata Prefecture, Japan, Earthquake Inferred from Waveform Inversion with Dense Strong-Motion Data, *Bulletin of the Seismological Society of America*, Vol. 99, No. 1, pp. 123–140, 2009. https://doi.org/10.1785/0120080257

24) Asano, K. and Iwata, T.: Source Process and Near-Source Ground Motions of the 2005 West Off Fukuoka Prefecture Earthquake, *Earth, Planets and Space*, Vol. 58, pp. 93–98, 2006. https://doi.org/10.1186/BF03351920

25) Asano, K. and Iwata, T.: Source Rupture Process of the 2007 Noto Hanto, Japan, Earthquake Estimated by the Joint Inversion of Strong Motion and GPS Data, *Bulletin of the Seismological Society of America*, Vol. 101, No. 5, pp. 2467–2480, 2011. http://dx.doi.org/10.1785/0120100254

26) Cirella, A., Piatanesi, A., Tinti, E. and Cocco, M.: Rupture Process of the 2007 Niigata-Ken Chuetsu-Oki Earthquake by Non-Linear Joint Inversion of Strong Motion and GPS Data, *Geophysical Research Letters*, Vol. 35, L16306, 2008. https://doi.org/10.1029/2008GL034756

27) Asano, K. and Iwata, T.: Characterization of Stress Drops on Asperities Estimated from the Heterogeneous Kinematic Slip Model for Strong Motion Prediction for Inland Crustal Earthquakes in Japan, *Pure and Applied Geophysics*, Vol. 168, No. 1, pp. 105–116, 2011. https://doi.org/10.1007/s00024-010-0116-y

28) Suzuki, W., Aoi, S. and Sekiguchi, H.: Rupture Process of the 2008 Northern Iwate (Iwate-Ken Engan-Hokubu) Earthquake Derived from Strong-Motion Records, 2008 (in Japanese, title translated by the authors). https://www.kyoshin.bosai.go.jp/kyoshin/topics/iwate_20080724/inversion/ (last accessed on October 13, 2021)

29) Suzuki, W. and Aoi, S.: Rupture Process of the 2009 Suruga-Bay Earthquake Derived from Near-Source Strong-Motion Records, 2009 (in Japanese, title translated by the authors). https://www.kyoshin.bosai.go.jp/kyoshin/topics/surugawan_20090811/inversion/ (last accessed on October 13, 2021)

30) Yagi, Y. and Fukahata, Y.: Rupture Process of the 2011 Tohoku-Oki Earthquake and Absolute Elastic Strain Release, *Geophysical Research Letters*, Vol. 38, L19307, 2011. https://doi.org/10.1029/2011GL048701

31) Kubo, H., Asano, K. and Iwata, T.: Source-Rupture Process of the 2011 Ibaraki-Oki, Japan, Earthquake (Mw 7.9) Estimated from the Joint Inversion of Strong-Motion and GPS Data: Relationship with Seamount and Philippine Sea Plate, *Geophysical Research Letters*, Vol. 40, pp. 3003–3007, 2013. https://doi.org/10.1002/grl.50558

32) Nagumo, H.: Study of the Rupture Process of the 2011 Northern Nagano Earthquake (Mj6.7), *Proceedings of the Annual Meeting of Japan Association for Earthquake Engineering*, pp. 328–329, 2012 (in Japanese, title translated by the authors).

33) Oana, A., Dan, K., Miyakoshi, J., Ishikawa, K. and Fukushi, T.: Evaluation of Strong Ground Motions of the 2011 Off Miyagi, Japan, Intra-Slab Earthquake at Onagawa by Empirical Green's Function Method Using Some Elemental Earthquakes, *Proceedings of the Seismological Society of Japan Fall Meeting*, p. 205, 2015 (in Japanese).

34) Tanaka, M., Asano, K., Iwata, T. and Kubo, H.: Source Rupture Process of the 2011 Fukushima-Ken Hamadori Earthquake: How Did the Two Subparallel Faults Rupture?, *Earth, Planets and Space*, Vol. 66, No. 101, 2014. https://doi.org/10.1186/1880-5981-66-101

35) Hikima, K.: Source Process and Strong Ground Motions of the February 25, Tochigi-Ken Hokubu

Earthquake, *Proceedings of the Annual Meeting of Architectural Institute of Japan*, Structural Engineering II, pp. 323–324, 2013 (in Japanese).

36) Ikeda, T., Konagai, K., Kamae, K., Sato, T. and Takahashi, Y.: Damage Investigation and Source Characterization of the 2014 Northern Part of Nagano Prefecture Earthquake, *Journal of Japan Society of Civil Engineers*, Ser. A1 (Structural Engineering & Earthquake Engineering), Vol. 72, No. 4, pp. I_975–I_983, 2016 (in Japanese).   https://doi.org/10.2208/jscejseee.72.I_975

37) National Research Institute for Earth Science and Disaster Prevention: Rupture Process of the 2015 Miyagi-Oki Earthquake Derived from Near-Source Strong-Motion Records, *Report of the Coordinating Committee for Earthquake Prediction, Japan*, Vol. 94, pp. 64–70, 2015 (in Japanese).

38) National Research Institute for Earth Science and Disaster Resilience: Rupture Process of the 2016 Urakawa-Oki Earthquake Derived from Near-Source Strong-Motion Records, *Report of the Coordinating Committee for Earthquake Prediction, Japan*, Vol. 96, pp. 47–51, 2016 (in Japanese).

39) Asano, K.: Source Modeling of an Mw 5.9 Earthquake in the Nankai Trough, Southwest Japan, Using Offshore and Onshore Strong-Motion Waveform Records, *Bulletin of the Seismological Society of America*, Vol. 108, No. 3A, pp. 1231–1239, 2018. https://doi.org/10.1785/0120170357

40) Kubo, H., Suzuki, W., Aoi, S. and Sekiguchi, H.: Source Rupture Processes of the 2016 Kumamoto, Japan, Earthquakes Estimated from Strong-Motion Waveforms, *Earth, Planets and Space*, Vol. 68, No. 161, 2016. https://doi.org/10.1186/s40623-016-0536-8

41) Asano, K. and Iwata, T.: Source Rupture Processes of the Foreshock and Mainshock in the 2016 Kumamoto Earthquake Sequence Estimated from the Kinematic Waveform Inversion of Strong Motion Data, *Earth, Planets and Space*, Vol. 68, No. 147, 2016. https://doi.org/10.1186/s40623-016-0519-9

42) Kubo, H., Suzuki, W., Aoi, S. and Sekiguchi, H.: Source Rupture Process of the 2016 Central Tottori, Japan, Earthquake (M_{JMA} 6.6) Inferred from Strong Motion Waveforms, *Earth, Planets and Space*, Vol. 69, No. 127, 2017. https://doi.org/10.1186/s40623-017-0714-3

43) National Research Institute for Earth Science and Disaster Resilience: Rupture Process of the 2016 off Fukushima Prefecture Earthquake Derived from Near-Source Strong-Motion Records, *Report of the Coordinating Committee for Earthquake Prediction, Japan*, Vol. 98, pp. 58–61, 2017 (in Japanese).

44) Fisher, A., Rudin, C. and Dominici, F.: All Models are Wrong, but Many are Useful: Learning a Variable's Importance by Studying an Entire Class of Prediction Models Simultaneously, *Journal of Machine Learning Research*, Vol. 20, No. 177, pp. 1–81, 2019. https://doi.org/10.48550/arXiv.1801.01489

45) Oana, A., Ishii, T. and Wada, K.: Applicability of Features to Ground Motion Evaluation Models Utilizing Machine Learning, *The 34th Annual Conference of the Japanese Society for Artificial Intelligence*, 3Rin4-03, 2020 (in Japanese).

46) Sammon, J. W.: A Nonlinear Mapping for Data Structure Analysis, *IEEE Transactions on Computers*, Vol. C-18, No. 5, pp. 401–409, 1969. https://doi.org/10.1109/T-C.1969.222678

47) Si, H. and Midorikawa, S.: New Attenuation Relationships for Peak Ground Acceleration and Velocity Considering Effects of Fault Type and Site Condition, *Journal of Structural and Construction Engineering* (Transactions of AIJ), Vol. 64, No. 523, pp. 63–70, 1999 (in Japanese). https://doi.org/10.3130/aijs.64.63_2

48) Takemura, M.: Magnitude–Seismic Moment Relations for the Shallow Earthquakes in and around Japan, *Journal of the Seismological Society of Japan*, 2nd ser., Vol. 43, pp. 257–265, 1990 (in Japanese).

49) Japan Meteorological Agency: Earthquake Information (in Japanese). http://www.jma.go.jp/jp/quake/quake_singendo_index.html (last accessed on October 13, 2021)

50) Asano, K., Iwata, T. and Hallo, M.: Source Rupture Process of the 2018 Northern Osaka Earthquake Estimated by Strong Motion Waveforms, *Proceedings of the Seismological Society of Japan Fall Meeting*, S24-09, 2018 (in Japanese).

51) National Research Institute for Earth Science and Disaster Resilience: Rupture Process of the 2019 off Yamagata Prefecture Earthquake Derived from Near-Source Strong-Motion Records, *Report of the Coordinating Committee for Earthquake Prediction, Japan*, pp. 73–77, Vol. 103, 2020 (in

Japanese).

52) Kubo, H., Suzuki, W., Aoi, S. and Sekiguchi, H.: Rupture Process of the Mj 7.3, February 13, 2021, Coast off Fukushima Prefecture Earthquake Derived from Strong-motion Data, 2021 (in Japanese, title translated by the authors). https://www.kyoshin.bosai.go.jp/kyoshin/topics/FukushimakenOki_20210213/inversion/inv_index.html (last accessed on October 13, 2021)

53) Yamada, M., Fukushima, Y. and Suetomi, I.: Building Damage During the 2008 Iwate-Miyagi Nairiku Earthquake, *Annuals of Disaster Prevention Research Institute*, *Kyoto University*, No. 52B, pp. 241–247, 2009 (in Japanese).

54) Takai, N. and Shigefuji, M.: Strong Motion Spatial Distribution Characteristics of off Fukushima Earthquakes: A Case Study on the February 13, 2021 and Similar Magnitude Earthquakes, *Proceedings of the Annual Meeting of Architectural Institute of Japan*, Structural Engineering II, pp. 291–292, 2021 (in Japanese).